Automotive and Engine Technology (2022) 7:179–196
https://doi.org/10.1007/s41104-022-00108-6

ORIGINAL PAPER

Numerical optimisation of the diffuser in a typical turbocharger compressor using the adjoint method

Kristaq Hazizi[1] · **Ahad Ramezanpour**[1] · **Aaron Costall**[2]

Received: 12 August 2021 / Accepted: 29 March 2022 / Published online: 23 April 2022

Abstract

In the automotive industry, the demand for fuel economy and emission reduction has resulted in engine downsizing, with turbochargers playing a key role in compensating for the performance loss. To be effective, a turbocharger's compressor must be accurately designed to match the engine's requirements. This study presents a novel non-parametric optimisation of the turbocharger compressor diffuser based on the compressor efficiency. The numerical models are based on the validation and mesh dependency study against experimental data from three points on each speed line of 150,000 (rpm) and 80,000 (rpm). The geometry and case data are related to the TD025-05T4 compressor from the 1.2-L Renault Megane passenger car. The turbocharger compressor diffuser geometry was optimised using the adjoint solver method within ANSYS FLUENT 2019 R1. The adjoint solver provides a gradient-based optimisation that can automatically create a series of iterations of a design, so that the mesh gradually deforms into an optimal shape to achieve a single target, the compressor efficiency in this study. The study considers a total of six operating cases on the compressor map to optimise the full and partial load compressor operations, leading to a real-world drive cycle. These cases are the three cases (closer to surge, stable midpoint, and closer to the choke point) on each of the speed lines. A typical result for mid-stable operation on a 150,000 (rpm) speed line shows a gradual increase in efficiency up to a maximum of 2.6% improvement. The optimal diffuser geometry impacts the overall car engine efficiency for real-world drive cycles, increasing power output and improving thermal efficiency.

Keywords Turbocharger compressor · *k*-Omega SST turbulence · Compressor efficiency · Compressor performance · Optimisation · Adjoint solver

List of symbols

π	Compression ratio
$P_{\text{out},t}$	Total outlet pressure
$P_{\text{in},t}$	Total inlet pressure
$T_{\text{out},t}$	Total outlet temperature
$T_{\text{in},t}$	Total inlet temperature
η_{tt}	Total to total compressor efficiency
Υ	Specific heat capacity ratio
λ	Thermal conductivity
ρ	Density
P	Static pressure
τ	Viscous stress
ω	Turbulence dissipation rate
$\mathbf{E}$	Energy
$\mathbf{h}$	Enthalpy
$\mathbf{J}$	Quantity of interest, adjoint observable
$\mathbf{k}$	Turbulence kinetic energy
$\mathbf{k}$	Thermal conductivity
$\mathbf{L}$	Lagrangian equations
m	Mass
$\mathbf{N}$	Linear problems
μ	Viscosity
μ_{t}	Turbulence viscosity
$\dot{\boldsymbol{v}}$	Volume flow rate
C_p	Specific heat capacity at constant pressure
$\underset{\sim}{q}$	Flow solution
$\underset{\sim}{c}$	Design variables
$\underset{\sim}{R}_i$	Residuals of Navier–Stokes equations
$\boldsymbol{q}$	Lagrange multipliers
$i, j, m = 1, 2, 3$	Indices for the Cartesian coordinates
u_i, u_j, u_m	Velocity components
δij	Kronecker delta
σ_{ij}	Stress tensor
$(\tau_{ij})_{\text{eff}}$	Viscous stress tensor

✉ Kristaq Hazizi
kristaq.hazizi@gmail.com

[1] Faculty of Science and Engineering, Anglia Ruskin University, Chelmsford CM1 1SQ, UK

[2] Institute for Advanced Automotive Propulsion Systems (IAAPS), University of Bath, Claverton Down BA2 7AY, UK

Q	External heat sources
s	Entropy
T	Temperature
u	Velocity

Abbreviations

CFD	Computational fluid dynamics
3D	Three-dimensional
MRF	Multi-reference frame
RANS	Reynolds Averaged Navier–Stokes Equations
SST	Shear-Stress Transport

1 Introduction

In recent years, turbochargers have been widely used in both diesel and petrol engines to compensate for the downsizing of engines due to fuel economy and regulatory emission reductions. Accurate and effective numerical modelling of the turbochargers leads to better and faster optimisation of the turbocharger compressor design, impacting engine performance. Recent advances in additive manufacturing have opened opportunities for non-parametric optimisation methods of the various design elements.

Recent unsteady numerical studies on turbocharger compressors have focused on various flow, thermal, and aeroacoustic optimisation aspects of the compressors while achieving a reasonable accuracy of the global performance in steady state if possible. Zhao et al. [22] studied the effect of inlet distortion on turbocharger compressor performance. The results indicate that any inlet angle decreases the stable operation range of the compressor and shifts the choke point towards smaller flow rates. When compared to unsteady approaches that can capture the overall average flow features and trends, including the surge, the computational techniques based on the steady-state RANS implementation are relatively fast, robust, and affordable [4].

In this research, operating points close to choke or surge have been considered if a reasonable level of numerical convergence has been achieved. Despite its limitations, steady-state RANS modelling can be used to cover an impressive number of cases within the stable compressor operating conditions in a relatively short computational time (Sundström, [17], which is more suitable for the adjoint optimisation method.

Tosto et al. [18] analysed the flow field inside a turbocharger centrifugal compressor. Ansys CFX is used to carry out steady and transient simulations using the k-omega SST turbulence model. Backflow can be observed at the operating points in the surge region.

The findings of a genetic algorithm-based impeller optimisation study conducted by Moussavi Torshizi, Hajilouy Benisi and Durali [13] using one-passage CFD analysis show a 2.2-point increase in performance at the nominal point and an increased surge margin of the optimised impeller. Experimental research on turbocharger compressors is focused on understanding and delaying stall and surge phenomena that take place because of flow instability and limit the performance of the turbochargers [5, 9, 21, 23].

There are a limited number of numerical research models on the unsteady and 3D full domain compressors due to the high demand for computational resources. The flow evolution along a speed line is investigated using unsteady, three-dimensional flow simulations with a centrifugal compressor geometry and a ported shroud. In the direction of impeller rotation, the reversed flow exhibits swirling motion. This creates a globally swirling flow upstream of the impeller, influencing the flow incidence angles at the blades and, as a result, their efficiency [16]. Furthermore, there is 1D unsteady research carried out by De Bellis and Bontempo [2] that is validated against experimental data, indicating a satisfactory agreement, especially in terms of pulse frequency, amplitude, and global shape.

Tuechler et al. [19] applied a parametric optimisation approach, coupling the ANSYS CFX with a genetic algorithm in MATLAB. The goal was to maximise isentropic efficiency at a target operating point close to the surge while avoiding major performance degradation near the choke margin. Because of 13 geometrical parameters, the results indicated that the goal optimisation efficiency gain of 2% was improved by around 1.9%, with the output decrease near the choke line being insignificant. Experimental tests on the optimised compressor show a 1–2% improvement in the efficiency of the basic model, although peak efficiency is improved by 3.0%, while the choke line remains almost unchanged.

The parametric optimisation of the centrifugal turbocharger with a vaneless diffuser was investigated by Mojaddam and Pullen [12]. The criteria include the meridional geometry, the distribution of rotor blade angles, and the starting position of the main blades and splitters. The research gradually optimised both performance and pressure, which resulted in a 3% and 11% increase in the original configuration impeller.

The adjoint solver used in this study is a non-parametric smart design optimisation tool that is based on obtaining detailed sensitivity data for the performance of a fluid system with respect to localised geometrical changes by computing the derivatives of the optimisation objective quantity.

According to Othmer [15], the use of the adjoint method in the automotive industry has been limited due to the exclusive reliance of the car industry on commercial CFD software and the high complexity of the parts being optimised in the automotive industry.

The resulting computational grids will also lead to stability issues with joint simulations that have proved to be more responsive to mesh defects than general flow simulations. These problems can be partly resolved by limiting the adjoint equations [14].

With time, it has become increasingly common to use direct methods of design optimisation for turbomachinery in general applications, in particular for compressor blades and diffuser geometry. This has become possible with significant progress in optimisation algorithms, in particular the invention of adjoint gradient computing that provides objective sensitivity details at a lower computation cost. This allows first-order optimisation approaches to complex design problems to be applied [6].

This study aims to optimise the diffuser geometry by applying the adjoint solver to a typical turbocharger engine passenger car, covering six operating points on two different speed lines, including partial and full engine loads. The compressor efficiency and performance were set as the main objectives of the optimisation and the impact on overall engine performance is discussed.

2 Reynolds Averaged Navier–Stokes equations

The Reynolds Averaged Navier–Stokes conservation of mass, momentum, and energy in conjunction with the ideal gas law has been applied to the steady-state compressible flow in this study.

When considering compressible flows, the Favre decomposition, which is a generalisation of the Reynolds decomposition ($f = \bar{f} + f'$), takes density variations into account for compressible flow. Using $\tilde{f}$ Favre time-average of f and with f'' the fluctuating component, it should be able to be written as follows:

$$f = \tilde{f} + f'', \tag{1}$$

where

$$\tilde{f} = \frac{\overline{\rho f}}{\bar{\rho}}. \tag{2}$$

And

$$f^{\varepsilon} = -\frac{\overline{\rho' f'}}{\bar{\rho}}. \tag{3}$$

Therefore, the Reynolds Averaged Navier–Stokes equations are

Conservation of Mass

$$\frac{\partial}{\partial_t}\left(\bar{\rho}\tilde{u}_i\right) = 0. \tag{4}$$

Conservation of Momentum

$$\frac{\partial(\bar{\rho}\tilde{u}_i)}{\partial_t} + \frac{\partial(\bar{\rho}\tilde{u}_i\tilde{u}_j)}{\partial_{x_j}} = -\frac{\partial\bar{p}}{\partial_{x_i}} + \frac{\partial\tilde{\sigma}_{ij}}{\partial_{x_j}} + \frac{\partial\tau_{ij}}{\partial_{x_j}}. \tag{5}$$

Conservation of Energy

$$\begin{aligned}&\frac{\partial}{\partial_t}\left(\bar{\rho}\left(\tilde{e} + \frac{\tilde{u}_i\tilde{u}_j}{2}\right) + \frac{\overline{\rho u_i'' u_i''}}{2}\right) + \frac{\partial}{\partial_{x_j}}\left(\bar{\rho}\tilde{u}_j\left(\tilde{h} + \frac{\tilde{u}_i\tilde{u}_i}{2} + \tilde{u}_j\frac{\overline{\rho u_i'' u_i''}}{2}\right)\right)\\ &= \frac{\partial}{\partial_{x_j}}\left(\tilde{u}_i\left(\tilde{\sigma}_{ij} - \overline{\rho u_i'' u_i''}\right)\right) + \frac{\partial}{\partial_{x_j}}\left(-\bar{q}_j - \overline{\rho u_j'' h_i''} + \overline{\sigma_{ij}u_i''} - \overline{\rho u_j''\frac{u_i'' u_j''}{2}}\right).\end{aligned} \tag{6}$$

The above set of equations are solved in conjunction with the ideal gas equation and the relationship between energy and temperature of the gas [18].

3 Eddy-viscosity models

The Reynolds stress tensor can be modelled using the Boussinesq Eddy-viscosity model, which relates the Reynolds stress tensor to the time-averaged velocity gradients defined by the eddy-viscosity closure model for conservation of momentum

$$-\overline{\rho u_i'' u_i''} = 2\mu_T S_{ij} - \frac{2}{3}\mu_T S_{kk}\delta_{ij}. \tag{7}$$

Eddy-viscosity closure for conservation of energy is written as [8]

$$\frac{\partial}{\partial_t}(\rho h) + \frac{\partial}{\partial x_j}\left(\rho u_j h - \lambda\frac{\partial T}{\partial x_j} + \overline{\rho u_j' h'}\right) = Q. \tag{8}$$

Boussinesq proposed that the Reynolds Stresses τ_{ij} can be related to the mean velocity gradients by a turbulent (eddy) viscosity, $\boldsymbol{\mu_T}$. Here, Turbulence is characterized by isotropic eddy viscosity $\boldsymbol{\mu_T}$ which enhance mixing between various constituent of the flow [20]

$$\mu_t = \rho c_\mu V_t l_t. \tag{9}$$

In the equation above, the eddy viscosity is proportional to the product of density, eddy velocity scale (Vt), and eddy length scale (lt). If any two quantities (eddy length, time, and velocity scale) are known, then the third quantity can be computed from the other two quantities. Eddy viscosity $\boldsymbol{\mu_T}$ is a flow property, not a fluid property, in this case.

Therefore, $\boldsymbol{\mu_T}$ is the turbulent eddy viscosity and represents a local quantity of the flow, since it takes into account the transfer of momentum caused by turbulent eddies.

4 Menter SST k-omega model

The turbulence model is governed by Wilcox's K-Omega SST governing equations. In general, it models turbulence using transport equations for turbulence kinetic energy $K = \frac{\overline{u_i'' u_i''}}{2}$ and the specific dissipation Omega. The resulting K-Omega model takes the following form:

$$\left(\frac{\partial}{\partial_t} + \overline{u}_i \frac{\partial}{\partial_{x_j}}\right) K = P - C_\mu K\omega + \frac{\partial}{\partial_{x_j}}\left[\left(\nu + \frac{\nu_T}{\sigma_K}\right)\frac{\partial_K}{\partial_{x_j}}\right], \quad (10)$$

$$\left(\frac{\partial}{\partial_t} + \overline{u}_i \frac{\partial}{\partial_{x_j}}\right)\omega = \left((C_{\epsilon 1} - 1)\frac{\omega}{K}\right)P - (C_{\omega 2} - 1)C_\mu \omega^2 + \frac{\partial}{\partial_{x_j}} \left[\left(\nu + \frac{\nu_T}{\sigma_\omega}\right)\frac{\partial_\omega}{\partial_{x_j}}\right], \quad (11)$$

where C_μ, σ_K, $C_{\epsilon 1}$, and $C_{\omega 2}$ are modelling coefficients calibrated experimentally.

Turbulent viscosity is defined as $\nu_T = \frac{K}{\omega}$, while production of turbulent kinetic energy P and specific dissipation rate omega are defined as follows:

$$P = -\overline{u'_i u'_j}\frac{\partial \overline{u_i}}{\partial_{x_j}} = 2\nu_T S_{ij} S_{ij}, \quad (12)$$

$$\omega = \frac{\nu}{C_\mu K}\overline{\frac{\partial u'_i}{\partial_{x_j}}\frac{\partial u'_i}{\partial_{x_j}}}. \quad (13)$$

Compared to other two-equation turbulence models, such as the *k*-epsilon one, the *k*-omega model shows some advantages. It provides better predictions of the boundary layer flows with pressure gradients. Also, *k*-omega ones can be integrated into the wall with small grid spacing ($y+ < 1$).

The main problem with this method is the treatment of turbulent interfaces, in particular at the boundary layer edge, which results in an unphysical sensitivity to the free-stream values of K and omega. In addition, the onset and amount

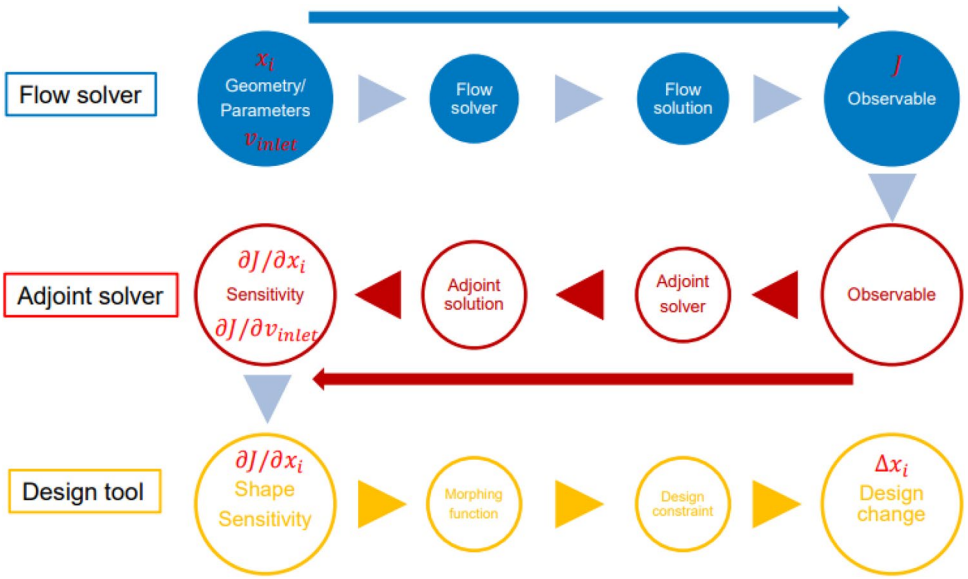

Fig. 1 Adjoint solver design workflow, one full cycle [3]

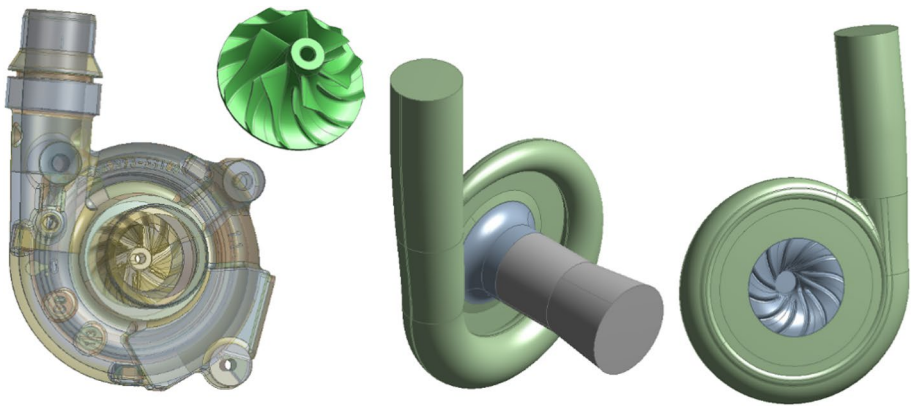

Fig. 2 Design geometry and computational domain

of flow separation under adverse pressure gradients are not well predicted.

To solve these problems, Menter [11] developed the Shear-Stress-Transport (SST) K-omega model, which corrects the deficiencies of the standard K-omega model through the addition of cross-difiusion terms and production limiters into the formulation of the eddy-viscosity. Due to its ability to capture flow separation, this model has been adopted for this research.

5 Overview of the adjoint method

The adjoint solver provides a gradient-based optimisation that can automatically create a series of iterations of a design, so that the mesh gradually deforms into an optimal shape to achieve single goals or multiple goals under multiple operating conditions. Its purpose is to calculate the derivative of an engineering quantity via a single calculation in relation to all the inputs to the system. The engineering quantity of interest, or single objective adjoint observable in this paper, is the compressor efficiency.

Figure 1 shows the adjoint base design workflow for one design change cycle. Each cycle includes three sections: flow, adjoint solvers, and design change, respectively. The equations for the adjoint solver are as follows.

Let us define the quantity of interest (adjoint observable is efficiency in this study), J, flow solution, $\underline{q}$ and inputs to the problem (flow/design variables)$\underline{c}$ [1],

$$J\left(\underline{q}(\underline{c}), \underline{c}\right), \tag{14}$$

$$R_i\left(\underline{q}(\underline{c}), \underline{c}\right) = 0. \tag{15}$$

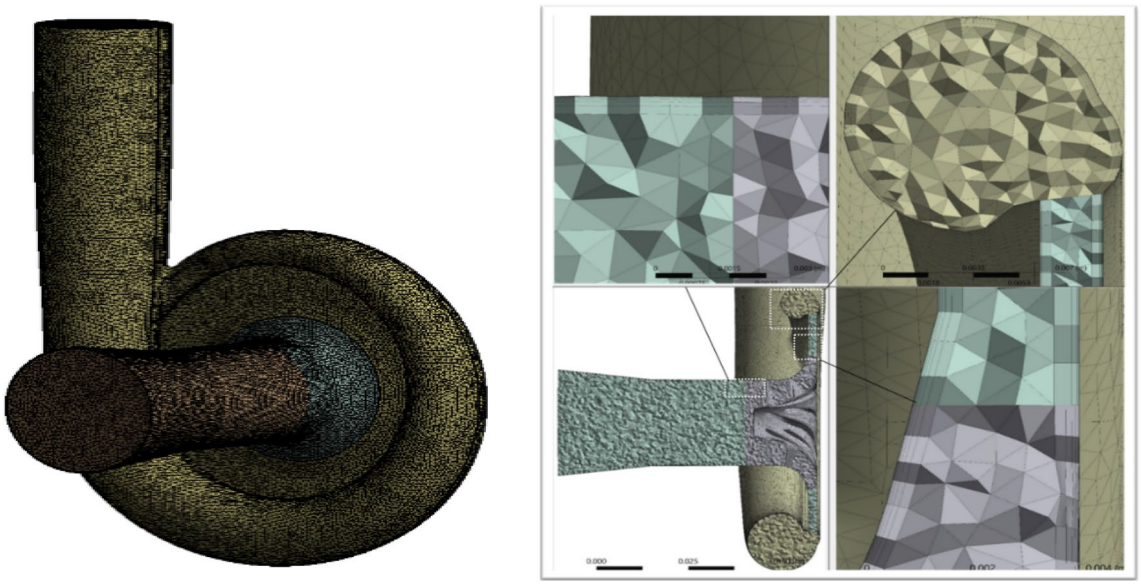

Fig. 3 Sample domain and boundary layer mesh, case 3 M

Table 1 Mesh study sizing for various cases, Speed line 150,000, Central zone

Central zone speed 150,000 (RPM)										
Case size (million)	First mesh height Y (mm)	Total mesh number	Efficiency	Torque (Nm)	Y Plus					
					Diffuser	Inlet	Inlet wall	Outlet	Volute	Impeller
1.6	0.001	1.699	0.756	0.184	0.1–0.6	0–0.25	0.1–1.4	0–0.35	0–8	0–7.5
2	0.001	2.077	0.757	0.184	0.1–0.7	0–0.25	0.1–1.6	0–0.55	0.-9	0–5.5
2.5	0.001	2.536	0.756	0.184	0.1–1	0–0.25	0–0.55	0–0.25	0–7	0–4.5
3	0.001	3.007	0.759	0.183	0.15–0.75	0–0.25	0.1–0.6	0–0.20	0.4	0–4.5
3.6	0.00005	3.681	0.757	0.184	0.01–0.035	0–0.014	0.05–0.01	0–0.01	0–3.5	0–1.4
3.8	0.00001	3.785	0.761	0.184	0.001–0.006	0–0.0025	0.02–0.045	0–0.002	0–3.5	0–1.4

Table 2 Experimental data from Mitsubishi Turbocharger and Engine Europe (MTEE)

Operating points	Impeller angular velocity (rpm)	Volume flow rate (m^3/s)	Output over input total pressure ratio, π	Compressor normalised efficiency
1 Surge	150,000	0.01840	1.70542	0.93
2 Central	150,000	0.04204	1.65297	1
3 Choke	150,000	0.06816	1.25516	0.61
4 Surge	80,000	0.00813	1.18696	0.844
5 Central	80,000	0.02130	1.15564	0.935
6 Choke	80,000	0.03490	1.07014	0.610

Next, consider the total derivatives of both the objective function J and the governing equations, R_i. These are written as follows:

We define the Lagrangian L with the vector of Lagrange multipliers $\tilde{\underline{q}}$

$$L\left(\underline{q}\left(\underline{c}\right),\underline{c},\tilde{\underline{q}}\right)=J+\tilde{\underline{q}}^{T}R. \tag{16}$$

Lagrange multipliers $\tilde{\boldsymbol{q}}=[u, v, w, p, T]$ is the adjoint variable.

Since $R=0$ everywhere, $\tilde{\boldsymbol{q}}$ can be arbitrarily chosen

$$L\left(\underline{q}\left(\underline{c}\right),\underline{c},\tilde{\underline{q}}\right)=J, \tag{17}$$

and, therefore, the derivatives of the observable J (Efficiency) related to design variables can be written as follows:

$$\frac{dJ}{d\underline{c}}=\frac{dL}{d\underline{c}}=\frac{\partial J}{\partial\underline{q}}\frac{d\underline{q}}{d\underline{c}}+\frac{\partial J}{\partial\underline{c}}+\tilde{\underline{q}}^{T}\left[\frac{\partial R}{\partial\underline{q}}\frac{d\underline{q}}{d\underline{c}}+\frac{\partial R}{\partial\underline{c}}\right]+\frac{d\tilde{\underline{q}}^{T}}{d\underline{c}}R. \tag{18}$$

If $\frac{d\tilde{\underline{q}}^{T}}{d\underline{c}}R=0$ is zero, then the above equation changes to

$$\frac{dJ}{d\underline{c}}=\frac{d\underline{q}}{d\underline{c}}\left(\frac{\partial J}{\partial\underline{q}}+\tilde{\underline{q}}^{T}\frac{\partial R}{\partial\underline{q}}\right)+\frac{\partial J}{\partial\underline{c}}+\tilde{\underline{q}}^{T}\frac{\partial R}{\partial\underline{c}}. \tag{19}$$

If we choose $\tilde{\underline{q}}$, such that (AdjointEquation)

$$\frac{\partial J}{\partial\underline{q}}+\tilde{\underline{q}}^{T}\frac{\partial R}{\partial\underline{q}}=0. \tag{20}$$

Sensitivity of observation (Efficiency) to design variables

$$\frac{dJ}{d\underline{c}}=\frac{\partial J}{\partial\underline{c}}+\tilde{\underline{q}}^{T}\frac{\partial R}{\partial\underline{c}}, \tag{21}$$

where $\tilde{\underline{q}}$ is the solution of the adjoint equation, and it can be written in a transpose equation as follows [10]: (Adjoint Equation, transpose equation)

$$\left[\frac{\partial R}{\partial\underline{q}}\right]^{T}\tilde{\underline{q}}=-\left[\frac{\partial J}{\partial\underline{q}}\right]^{T}. \tag{22}$$

6 Numerical settings

A three-dimensional turbocharger compressor at atmospheric operating pressure, and an ambient temperature of 20 °C is simulated, which is consistent with the experimental

Table 4 Adjoint versus baseline results for all operating points

Map area	Speed line (rpm)	Compressor efficiency		Improvement (%)
		Baseline	Adjoint	
SURGE	CASE 1 (150,000)	0.729	0.746	2.44
CENTRAL	CASE 2 (150,000)	0.759	0.779	2.63
CHOKE	CASE 3 (150,000)	0.503	0.530	5.36
SURGE	CASE 4 (80,000)	0.734	0.744	1.36
CENTRAL	CASE 5 (80,000)	0.767	0.777	1.3
CHOKE	CASE 6 (80,000)	0.506	0.510	0.79

Table 3 Baseline numerical efficiency results for all operating points

Case 3 M	Operating points					
	80,000 rpm			150,000 rpm		
	(Surge)	(Central)	(Choke)	(Surge)	(Central)	(Choke)
Baseline efficiency	0.734	0.767	0.506	0.729	0.759	0.503

Then

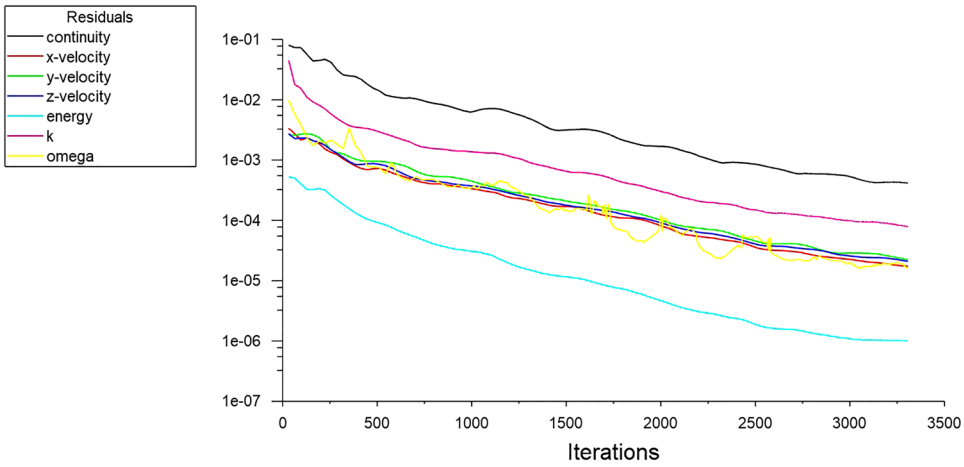

Fig. 4 A typical residual plot for the case of 3 M million mesh used in this study

conditions. The compressor housing, impeller, and extracted computational domain are shown in Fig. 2. The computational domain has been divided into four zones; inlet, diffuser, and outlet zones that are fixed (stationary) and a rotational zone in between, covering the impeller. The compressor flow is simulated through multiple reference frames (MRF), which are divided into flow domains in the rotation area of those reference frames, which rotate at the same speed as the impeller in rotation.

The flow in each moving cell zone is solved using the Moving Reference Frame equations.

For the mesh independency test of the diffuser optimisation purpose, six mesh sizes in total are initially considered in this research, with a constant first layer mesh thickness of 0.001 mm for the first four mesh cases. Instead, for the last two mesh cases of 3.6 and 3.8 mesh elements, the first layer thickness is 0.00005 mm and 0.00001 mm, respectively, as seen in the sample domain and boundary-layer mesh in Fig. 3. The approximate total mesh number of cases of 1.6, 2, 2.5, 3, 3.6, and 3.8 million domain cells is seen in Table 1. The growth rate of the boundary layer mesh is set at the recommended rate of 1.2 and 10 mesh layers are considered on volute, diffuser, inlet, and impeller walls.

An implicit pressure–velocity coupled solver is used with second-order discretisation for all flow, energy, and turbulence parameters. The green-Gauss node based is used for spatial discretisation where a weighted average of the cell values is constructed in each node to derivative, which is more accurate for unstructured tetrahedral cells. For accelerated convergence, a pseudo-transient approach was used, in which forms of implicit under-relaxation are controlled by pseudo time step size.

The $k = 0.0242$ W/(m.K) is considered constant thermal conductivity and the specific heat capacity is considered $Cp = 1006.43$ J/kg.K.

As the turbocharger compressor stage takes air from the atmosphere, atmospheric conditions are used. The inlet boundary of the compressor was set to the mass-flow rate and the outlet boundary was set as the pressure outlet at six different operating points considered in this research.

Based on the residual monitor plot shown in Fig. 4, all the equations are converged within the convergence tolerance. Also, it can be observed that the numerical efficiency and moment values represent a small change, which is negligible and not considered, as seen and summarised in Table 1. Then, it can be concluded after this mesh study that the values of numerical efficiency and moments are stable and do not depend on mesh refinement. Table 1 summarises the y plus values wherein most compressor areas have achieved a value of < 1 as expected, and in the areas of volute and impeller, they have reached a value < 5. The y plus values show that the numerical model solution is accurate and as expected. For further optimisation purposes of the diffuser geometry, it was selected case 3 M to follow the baseline and optimised geometry simulations.

The total pressure ratio and efficiency are verified as global variables with respect to the experimental data shown in Table 2. For this study, three operating points on a peak efficiency curve along a 150,000 rpm speed line and three points on partial load along an 80,000 rpm speed line are considered. The range of points was selected to cover diverse operating loads and variations in relation to the surge and choke lines of the compressor map.

The pressure ratio, π, is calculated as the ratio of total outlet to inlet pressures. The total-to-total efficiency, η_{tt}, is calculated as the isentropic ideal work input over the actual work input. The formulations for these parameters are

Total pressure ratio

$$\pi = \frac{P_{\mathrm{out},t}}{P_{\mathrm{in},t}}, \tag{23}$$

Total to total compressor efficiency

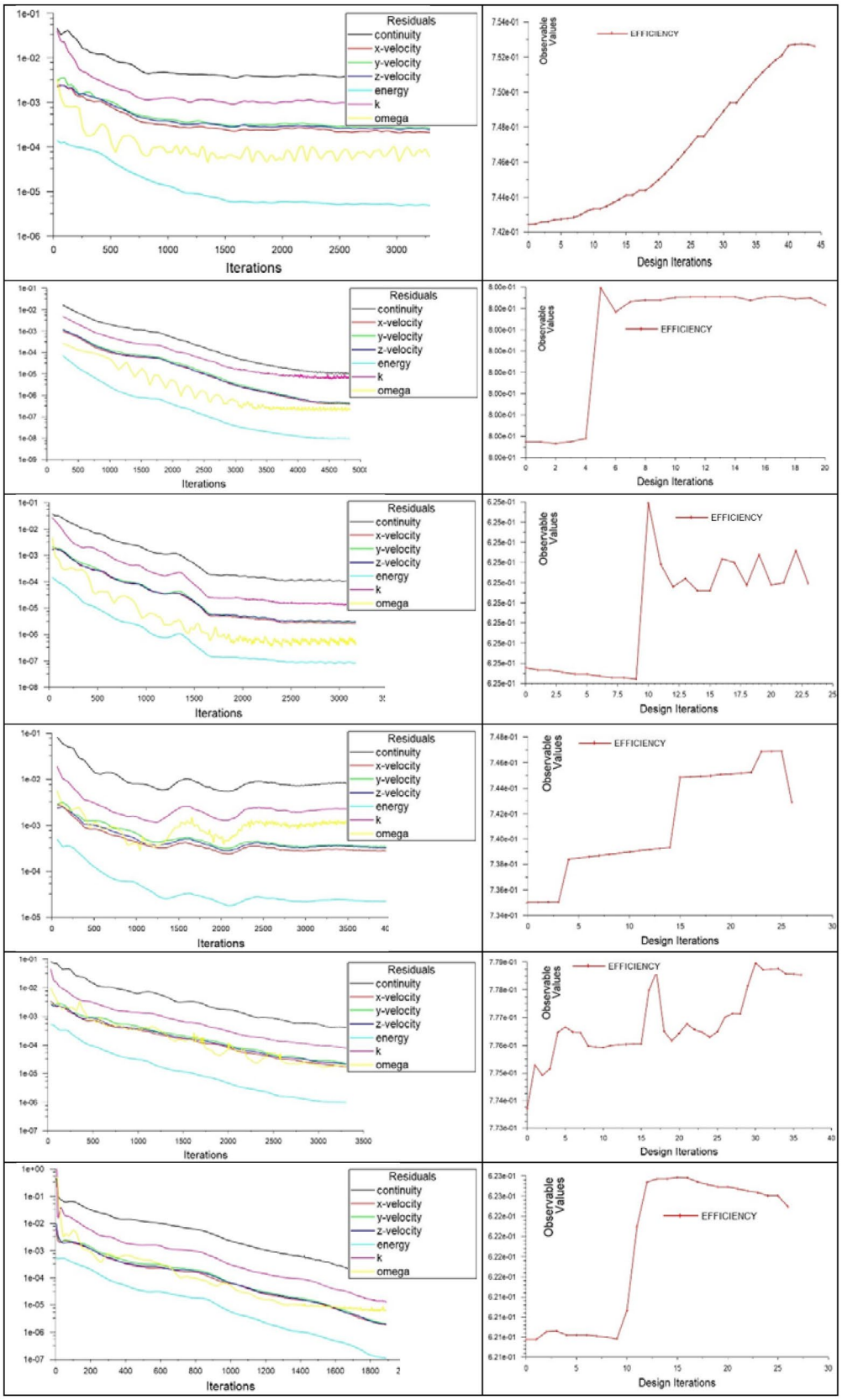

Fig. 5 Residual Monitors Plot Baseline (left column) and Adjoint design iterations (right column), Close to surge (top), Central (middle) and Close to choke (bottom), and Speed lines 80,000 rpm (up) and 150,000 rpm (down)

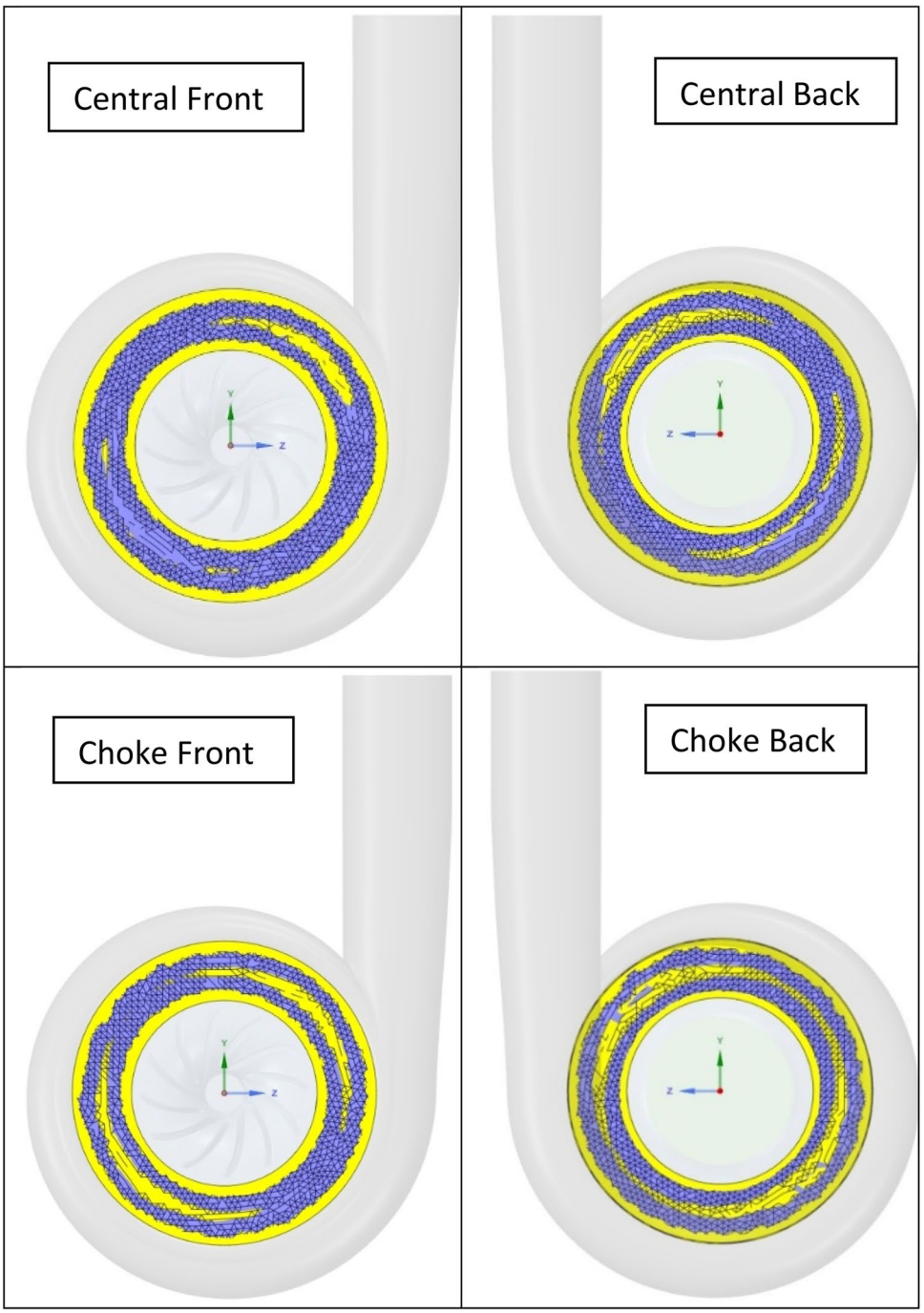

Fig. 6 Diffuser Geometry Changes, close to Surge, Central, and close to Choke area (Top, Middle and Bottom), Speedline 80,000 rpm

$$\eta_{tt} = \frac{\pi^{(\gamma-1)/\gamma} - 1}{\left(T_{\text{out},t}/T_{\text{in},t}\right) - 1}. \tag{24}$$

The predicted numerical efficiency result values achieved for the baseline diffuser geometry are summarised in Table 3.

In a recent research paper [7], they investigated and analysed the fluid domain of the same compressor about the pressure ratio and efficiency. The numerical result of a stable point selected close to the central area, speed line 150,000, has been compared with experimental data extracted from MTEE, validating the numerical model. Numerical analysis of pressure ratio and efficiency has been extended and compared with experimental data for all other design points of the compressor map selected. Further numerical simulations for optimisation purposes covering all design areas (6 cases) were performed in this study, comparing both the baseline and optimised compressor diffuser geometry.

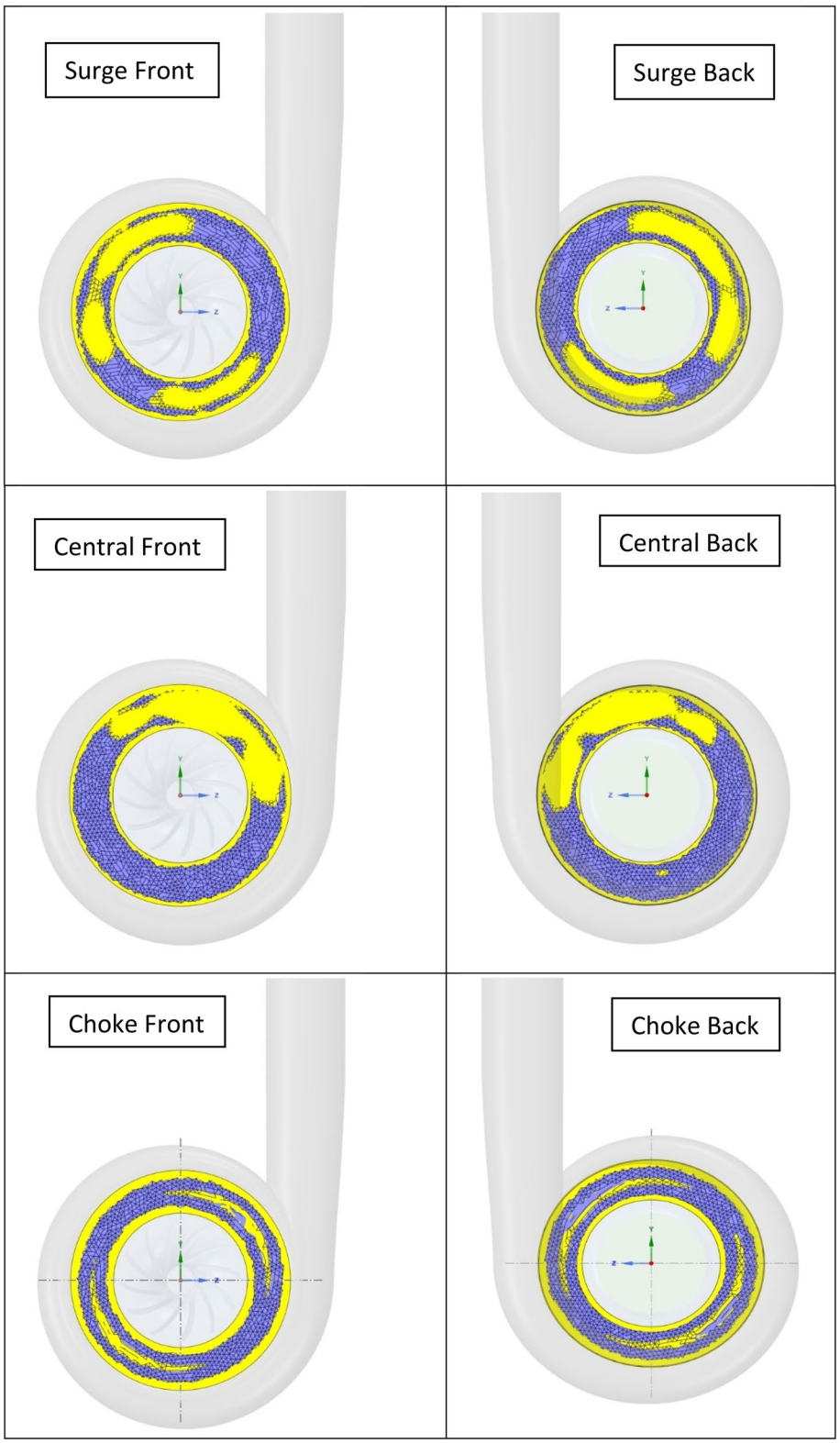

Fig. 7 Diffuser Geometry Changes, close to Surge, Central, and close to Choke area (Top, Middle and Bottom), Speedline 150,000 rpm

Table 5 Diffuser Geometry Change for Operating areas, close to Surge, central and close to choke, with a Speedline 80,000 (rpm) and 150,000 (rpm)

Volume (mm^3)		Difference (mm^3)
Baseline geometry	6253.861	
SURGE	5925.7379	− 328.1231
CENTRAL	6080.4786	− 173.3824
CHOKE	5585.0872	− 668.7738
SURGE	6048.0847	− 205.7763
CENTRAL	5592.6483	− 661.2127
CHOKE	5708.7985	− 545.0625

7 Results and discussion

The baseline and optimised diffuser geometry efficiency values and the improved percentage are shown in Table 4 for all the case studies. The predicted efficiency results of optimised diffuser geometry compared with baseline diffuser geometry show an increase in efficiency for all case studies. In particular, case areas with a speed line of 150,000 rpm, achieved an improvement of approximately 5.36% of efficiency value in the choke area.

It can be observed that the efficiency improvement is significant for the speed line at 150,000 rpm and the operating point close to the choke. That can be linked to the high mass-flow rate sensitivity to the change of diffuser geometry.

The residual plots for baseline and adjoint design iterations of optimised diffuser geometry, for all operating areas, are shown graphically in Fig. 5. The results of the optimisation achieved in this paper are based on the optimal local efficiency values at the operating points, as shown in Fig. 5, for each case study. It can be observed that the efficiency increases up to a certain design iteration, which is the maximum local efficiency value and then starts decreasing at that design iteration.

Figure 6 shows the geometry change of optimised diffuser geometry versus baseline geometry for operating areas surge, central, and choke, with a speed line 80,000 (rpm). Instead, Fig. 7 shows the geometry change of optimised diffuser geometry versus baseline geometry for operating areas surge, central, and choke, with a speed line of 150,000 (rpm).

To differentiate the geometry change, the baseline diffuser geometry is made yellow and the optimised diffuser geometry is made purple. There can be observed areas where the optimised geometry has shrunk. Instead, Table 5 shows the difference in geometry volume between the optimised diffuser geometry and the baseline diffuser geometry.

Figures 8 and 9 show the contours of absolute pressure and speed lines at 80,000 (rpm) and 150,000 (rpm), respectively, for both configurations; optimised diffuser geometry, and baseline diffuser geometry, at the diffuser middle cross-section.

Based on the result values obtained for the absolute pressure, shown in Figs. 8 and 9, for both configurations, speed lines of 80,000 rpm and 150,000 rpm, respectively, in the case area close to surge, it can be noticed that the maximum value of absolute pressure is increased in the optimised diffuser geometry. The maximum absolute pressure value for the case area close to surge in the speed line of 80,000 rpm is increased from 119,042 Pa (baseline) to 119,105 Pa (optimised diffuser geometry), and in the speed line of 150,000 rpm, it is increased from 170,029 Pa (baseline) to 170,070 Pa (optimised diffuser geometry).

Figures 8 and 9 show that for both speed lines, close to choke, the maximum value of absolute pressure is increased in the optimised diffuser geometry. The maximum absolute pressure value for the case area close to the choke, in the speed line of 80,000 rpm, is increased from 113,577 to 113,764 Pa and in the speed line of 150,000 rpm, it is increased from 144,739 to 144,764 Pa.

Furthermore, based on the result values obtained for the absolute pressure, shown in Figs. 8 and 9, for both configurations and both speed lines, it can be noticed that the maximum value of absolute pressure is increased in the optimised diffuser geometry in the central (middle) case study. The maximum absolute pressure value for the case area central (middle) in the speed line of 80,000 rpm is increased from 11,691 Pa (baseline) to 116,930 Pa (optimised diffuser geometry), and in the speed line of 150,000 rpm, it is increased from 165,541 Pa (baseline) to 171,535 Pa (optimised diffuser geometry).

It can be observed that the absolute pressure for both configurations of speed lines, 80,000 rpm and 150,000 rpm, increased radially at the exit of the diffuser geometry. Due to the variable and localised decreased flow section in the diffuser, the kinetic energy conversion to pressure has improved. The results show that localised optimisation due to the volute and exit geometry is effective in improving the performance of the compressor.

The absolute pressure results summarised in Table 6 are consistent with our expectations as the absolute pressure

Table 6 Absolute pressure contour value for all cases

Map area	Speed line (rpm)	Maximum absolute pressure (Pa)	
		Baseline	Adjoint
Surge	Case 1 (150,000)	170,029	170,070
Central	Case 2 (150,000)	165,541	171,535
Choke	Case 3 (150,000)	144,739	144,764
Surge	Case 4 (80,000)	119,042	119,105
Central	Case 5 (80,000)	116,911	116,930
Choke	Case 6 (80,000)	113,577	113,764

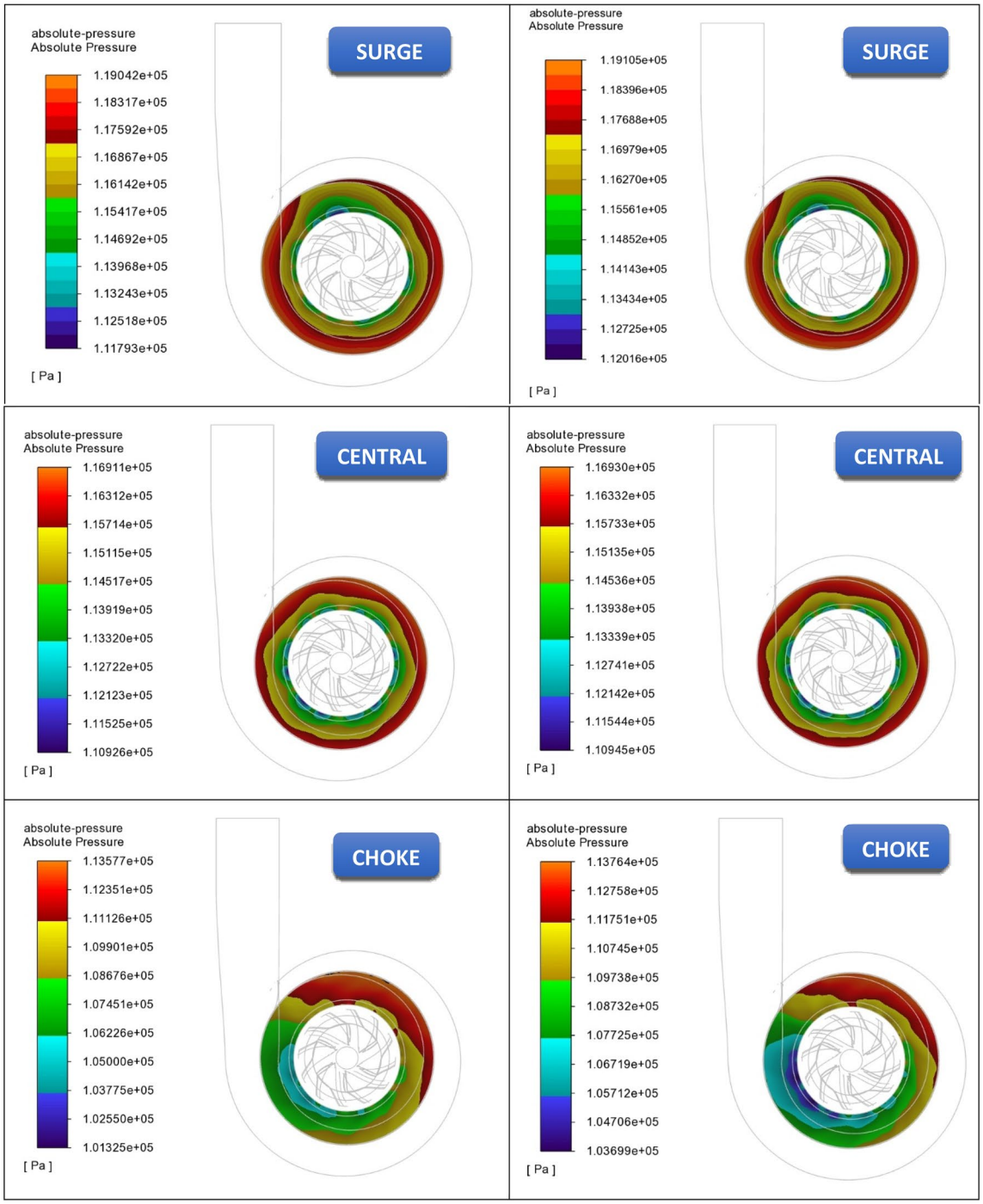

Fig. 8 Contours Absolute Pressure at diffuser middle cross-section, Speedline 80,000 rpm, close to surge (top), central (middle), and close to choke (bottom), Baseline (left) and Optimised diffuser geometry (right)

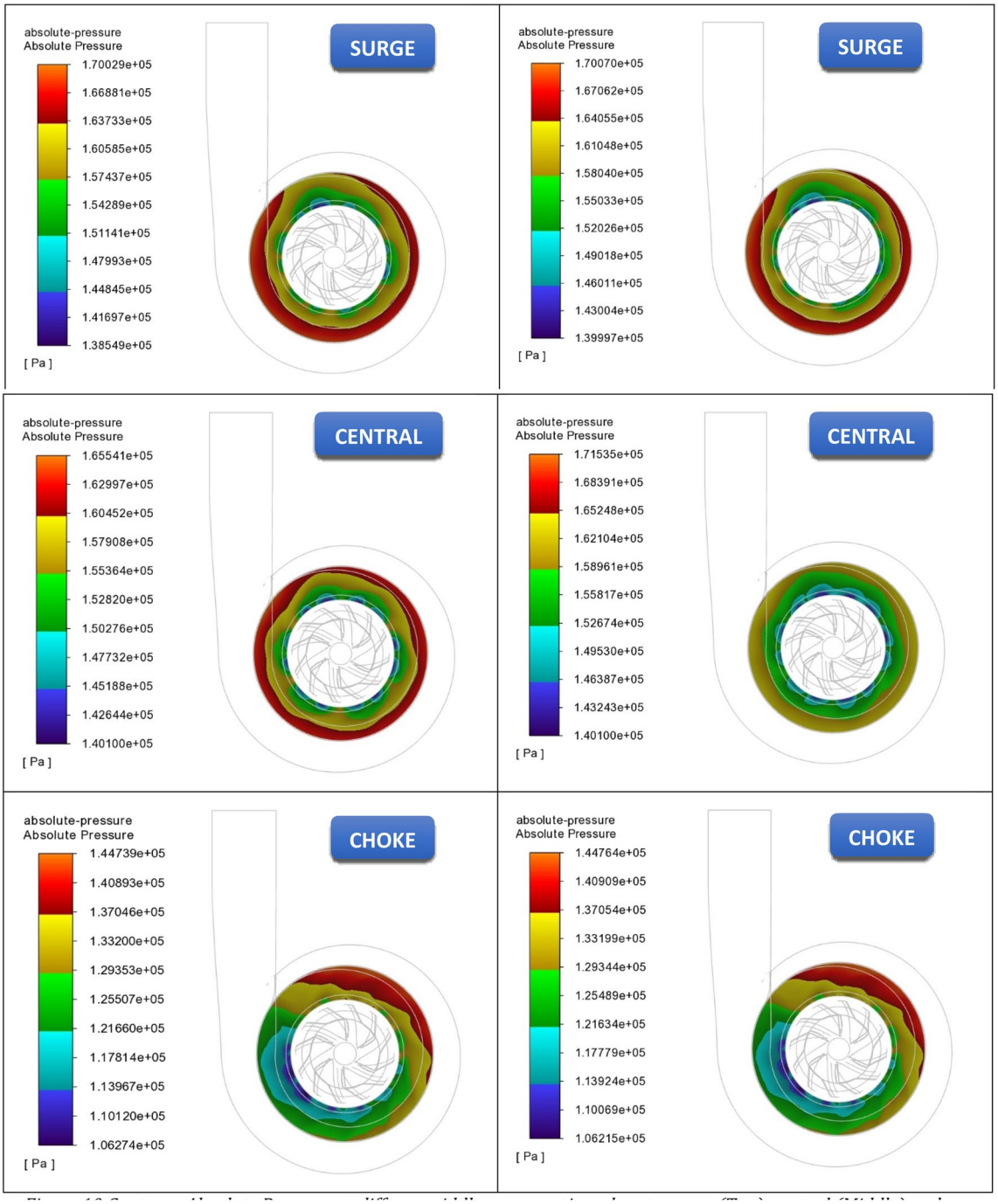

Fig. 9 Contours Absolute Pressure at diffuser middle cross-section, close to surge (top), central (middle), and close to choke (bottom), Speedline 150,000 rpm, Baseline (left) and Optimised diffuser geometry (right)

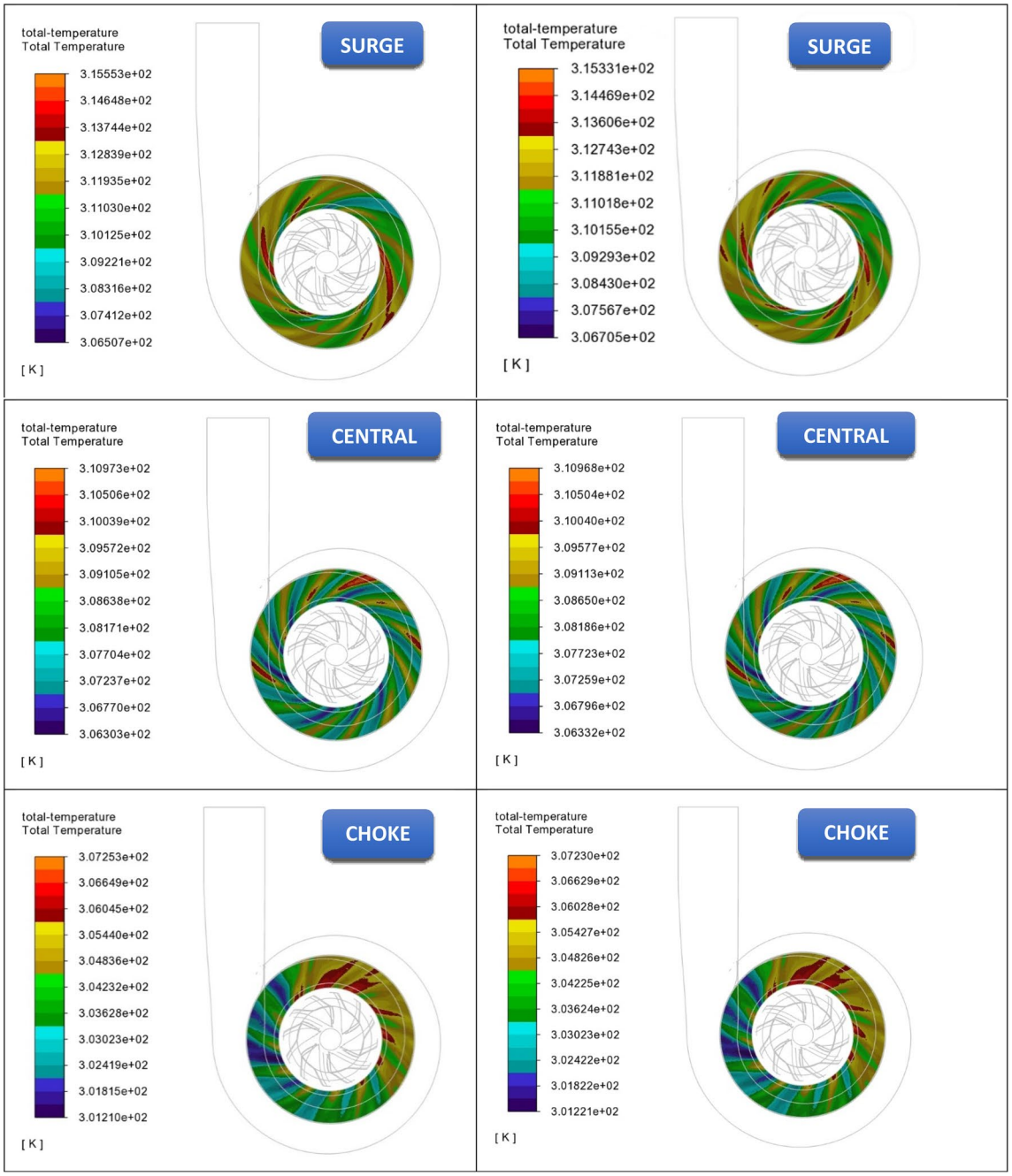

Fig. 10 Contours Total Temperature at diffuser middle cross-section, Speedline 80,000 rpm, close to surge (top), central (middle), and close to choke (bottom), Baseline (left) and Optimised (right) diffuser geometry

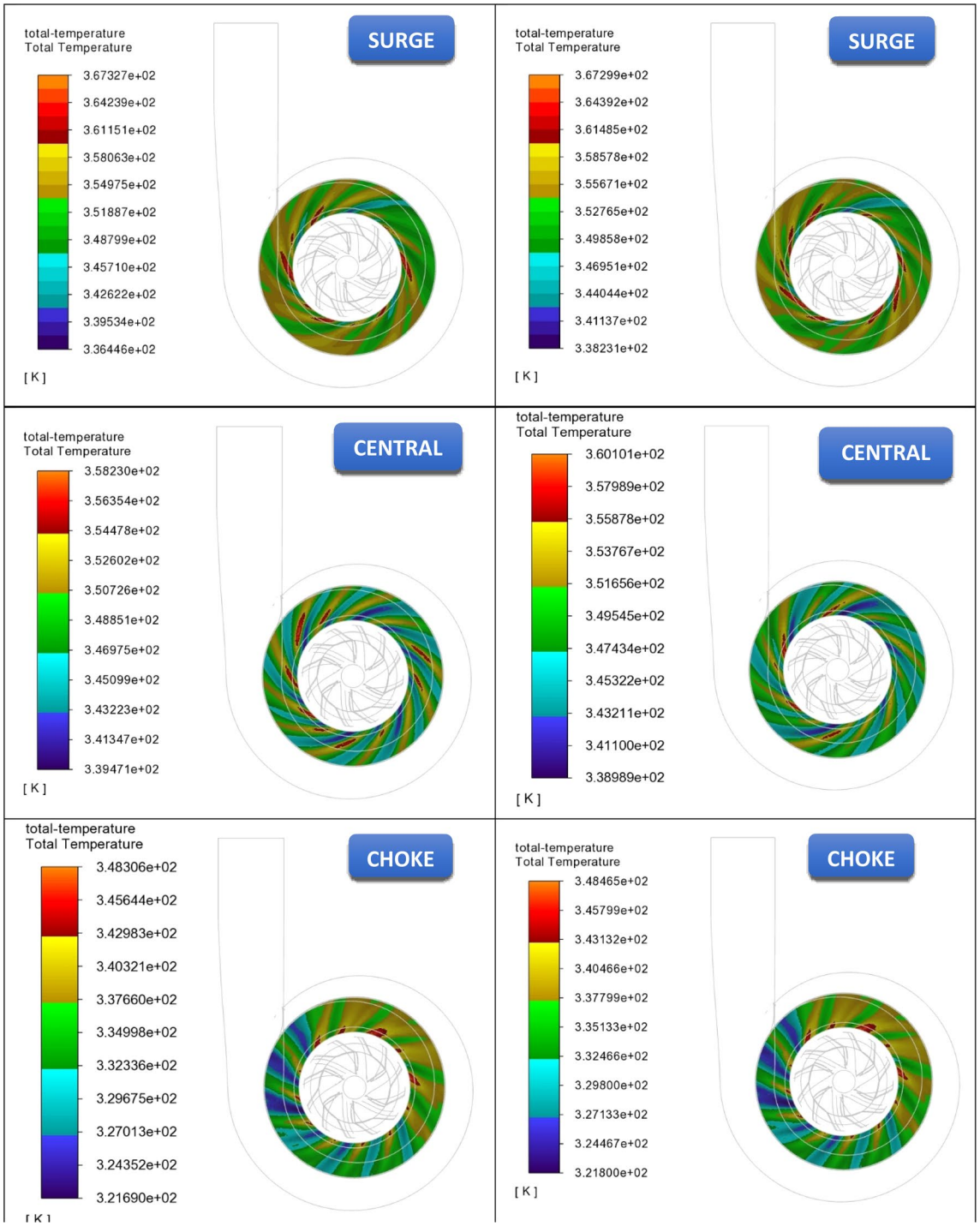

Fig. 11 Contours Total Temperature at diffuser middle cross-section, close to surge (top), central (middle), and close to choke (bottom), Speedline 150,000 rpm, Baseline (left) and Optimised diffuser geometry (right)

Table 7 Total temperature contour value for all cases

Map area	Speed line (rpm)	Maximum total temperature (K)	
		Baseline	Adjoint
Surge	Case 1 (150,000)	367.327	367.299
Central	Case 2 (150,000)	358.230	360.101
Choke	Case 3 (150,000)	348.306	348.465
Surge	Case 4 (80,000)	315.553	315.331
Central	Case 5 (80,000)	310.973	310.968
Choke	Case 6 (80,000)	307.253	307.230

values are increased in the optimised diffuser geometry versus the baseline diffuser geometry in all operating areas.

Figures 10 and 11 show the contours of total temperature for speed lines of 80,000 (rpm) and 150,000 (rpm) and, for both configurations, optimised and baseline diffuser geometry in the middle cross-section of the diffuser. For both speedlines, in the case of close to surge, it can be noticed that the maximum value of total temperature is decreased in the optimised diffuser geometry. The maximum total temperature value for the case area close to surge, in the speed line of 80,000 rpm, decreased from 315.553 to 315.331 K and in the speed line of 150,000 rpm, increased from 367.327 to 367.299 K.

Figures 10 and 11, for both configurations and speedlines in the case close to the choke, show that the maximum value of total temperature is decreased in the optimised diffuser geometry. The maximum total temperature value for the case close to the choke in the speed line of 80,000 rpm is decreased from 307.253 to 307.230 K, and in the speed line of 150,000 rpm, it is increased from 348.306 to 348.465 K.

Furthermore, Figs. 10 and 11, for both configurations and speed lines in case area central (middle), show that the maximum value of total temperature is decreased in the optimised diffuser geometry for the speed line of 80,000 rpm and increased for the speed line of 150,000 rpm. The maximum total temperature value for the case area central (middle) in the speed line of 80,000 rpm is decreased from 310.973 to 310.968 K and that in the speed line of 150,000 rpm is increased from 358.230 to 360.101 K.

It can be observed that while there is no pattern for maximum temperature values (Table 7), the changes are small and the improvement in efficiency is mostly due to the increased pressure ratio.

Therefore, based on Eq. 24, the efficiency value is linked to the variation of the absolute pressure in the numerator and the variation of the total temperature in the denominator. The results of efficiency in Table 4 show improvement across all case studies in this research. This increase has an impact on the engine's efficiency and the overall performance of a passenger car for real-world drive cycles, increasing power output and improving thermal efficiency.

Most of the turbocharger operation takes place in the stable area, the central area of 150,000 and 80,000 rpm (full and half load). Figures 6 and 7 show that the geometry change for optimisation of the central area is almost identical for both speed lines. A typical cross-section of the optimum geometry for case study number 2 has been shown in Fig. 12 for both the front and back of the diffuser geometry. The geometry has shrunk on either side of the diffuser, with the maximum shrinking point slightly closer to the diffuser inlet. Such a change in practical terms is possible with laser sintering techniques.

8 Conclusions

This study optimises the diffuser geometry in a passenger vehicle turbocharger compressor using a gradient-based solution approach employing a new non-parametrical adjoint shaping optimisation for ideal gas turbulent compressible flow applications. The novelty of this research is to adapt the adjoint solver to an observable quantity, compressor efficiency in this study, and link the associated solution to the surface adjoint sensitivity, leading to mesh morphing techniques to change the diffuser geometry and improve the compressor efficiency.

The step differentiation works well with the Jacobian equation approach to solve the RANS equations. The k-omega SST turbulence model for two speed lines of 150,000 and 80,000 rpm was developed with three cases for each speed line studied. The three cases include those close to choke, central (stable), and close to surge on the compressor map.

The following conclusions were obtained:

1. The efficiency values for all operating areas and speed lines increased; the maximum increase was 5.36% for the case close to the choke of the 150,000 rpm speed line.
2. While the geometry variation of the optimised diffuser is different for the cases close to the choke and surge optimisation, the geometry change is consistent in the stable central area for both speed lines. Therefore, the optimisation of the diffuser is possible for the real-world cycle (half and full load engine operation) for the majority of operational time.
3. The results show that the diffuser optimisation is possible by tightening the flow on either side of the diffuser close to the compressor exit and with the maximum airflow shrinking area slightly closer to the diffuser inlet.

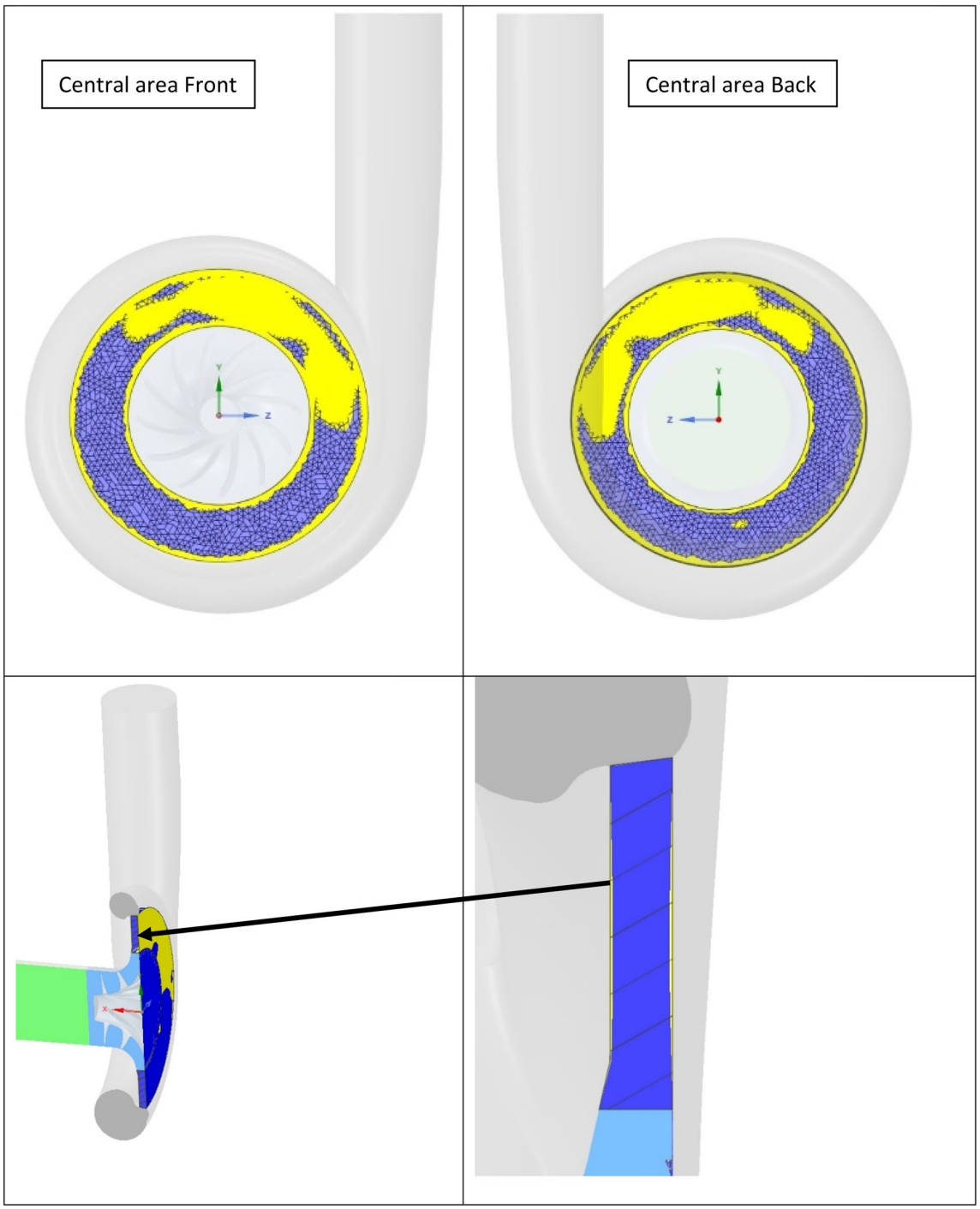

Fig. 12 Diffuser Geometry Changes Operating Central area, Speedline 150,000 rpm, 3D front view left side and 3D back view right side

4. Within the central areas (stable), the efficiency value improvement in both speed lines is in the range of 1.3–2.63%.

As a typical car engine runs at full and half load in the real world, the compressor should be more efficient, which should cut down on fuel consumption and emissions.

References

1. ANSYS: Lecture 01: Introduction ANSYS fluent adjoint solver. (2019)
2. De Bellis, V., Bontempo, R.: Development and validation of a 1D model for turbocharger compressors under deep-surge operation. Energy **142**, 507–517 (2018). https://doi.org/10.1016/j.energy.2017.10.045
3. Canonsburg, T.D.: Ansys fluent adjoint solver. Ratio **15317**, 724–746 (2012)
4. Dicholkar, A., Zahle, F., Sørensen, N.N.: Convergence enhancement of SIMPLE-like steady-state RANS solvers applied to airfoil and cylinder flows. J. Wind Eng. Ind. Aerodyn. (2022). https://doi.org/10.1016/j.jweia.2021.104863. Accessed 20 Dec 2021.
5. Gancedo, M., Guillou, E., Gutmark, E.: Effect of bleed slots on turbocharger centrifugal compressor stability. Int. J. Heat Fluid Flow **70**(70), 206–215 (2018). https://doi.org/10.1016/j.ijheatfluidflow.2017.12.007
6. Geuens, C.S.E.F.: AdjointBased Inverse Design of Axial Compressor Airfoils Development & Evaluation of a New Design Method. (2020). Available at: http://repository.tudelft.nl/.
7. Hazizi, K. et al.: Numerical analysis of a turbocharger compressor. In Mohamad, V, et al. (ed) E3S Web of Conferences, vol. 128. p. 06012 (2019). https://doi.org/10.1051/e3sconf/201912806012. Accessed 8 Nov 2019
8. Lo CD-adapco, S.: Lecture CFD-2 Introduction to CFD, Modelling of turbulence • Conservation equations • What is CFD • Solution method • CFD grids and boundary types • Turbulence models • Boron dilution transient • Pressure drop in spacer grid • Thermal stripping in T-junct. (2014). Available at: https://cfdisrael.blog/2021/10/04/eddy-viscosity-concept-turbulent-kinetic-energy-equation/
9. Marelli, S., et al.: Experimental analysis on the performance of a turbocharger compressor in the unstable operating region and close to the surge limit. Exp. Thermal Fluid Sci. **53**, 154–160 (2014). https://doi.org/10.1016/j.expthermflusci.2013.11.025
10. Mavriplis, D. J.:Adjoint-based sensitivity analysis for computational fluid dynamics. (2005)
11. Menter, F.R.: Two-equation eddy-viscosity turbulence models for engineering applications. AIAA J. **32**(8), 1598–1605 (1994). https://doi.org/10.2514/3.12149
12. Mojaddam, M., Pullen, K.R.: Optimization of a centrifugal compressor using the Design of Experiment technique. Appl. Sci. (Switzerland) (2019). https://doi.org/10.3390/app9020291
13. Moussavi Torshizi, S.A., Hajilouy Benisi, A., Durali, M.: Multilevel optimization of the splitter blade profile in the impeller of a centrifugal compressor. Scientia Iranica **24**(2), 707–714 (2017). https://doi.org/10.24200/sci.2017.4055
14. Mura, G. L.: Mesh Sensitivity Investigation in the Discrete Adjoint Framework (Issue March). (2017)
15. Othmer, C.: Adjoint methods for car aerodynamics. J. Math. Ind. **4**(1), 1–23 (2014). https://doi.org/10.1186/2190-5983-4-6
16. Semlitsch, B., Mihăescu, M.: Flow phenomena leading to surge in a centrifugal compressor. Energy **103**, 572–587 (2016). https://doi.org/10.1016/j.energy.2016.03.032
17. Sundström, E., Semlitsch, B., Mihăescu, M.: Similarities and differences concerning flow characteristics in centrifugal compressors of different size. Springer Proc. Phys. (2016). https://doi.org/10.1007/978-3-319-30602-5_57
18. Tosto, F.: Investigation of performance and surge behavior of centrifugal compressors through CFD simulations., (Issue March) (2018)
19. Tuechler, S, Chen, Z, Copeland, C.: Multipoint Optimisation of Radial Compressor Using Computational Fluid Dynamics and Genetic Algorithm. in GPPS-2018. (2018)
20. Tomer Avraham: Eddy Viscosity Concept: (2022). Available at: https://cfdisrael.blog/2021/10/04/eddy-viscosity-concept-turbulent-kinetic-energy-equation/. Accessed 4 Oct 2021
21. Xinqian, Z., Anxiong, L.: Experimental Investigation of Surge and Stall in a High-Speed Centrifugal Compressor. J. Propul. Power **31**(3), 815–825 (2015). https://doi.org/10.2514/1.B35448
22. Zhao, B., et al.: Impact of inlet distortion on turbocharger compressor stage performance. Appl. Therm. Eng. **124**, 393–402 (2017). https://doi.org/10.1016/j.applthermaleng.2017.05.181
23. Zheng, X., et al.: Experimental investigation of surge and stall in a turbocharger centrifugal compressor with a vaned diffuser. Exp. Thermal Fluid Sci. **82**, 493–506 (2017). https://doi.org/10.1016/j.expthermflusci.2016.11.036